ASIIMETRIK
JURNAL ILMIAH REKAYASA DAN INOVASI
p-ISSN: 2655-1861, **e-ISSN:** 2716-2923
Volume **8** Number **2**, **2026**

Flow Distribution Analysis in a Multi Inlet Gas Manifold Using Computational Fluid Dynamics

Jerico Justin, Abrar Riza*, Steven Darmawan
Universitas Tarumanagara, Jakarta, Indonesia
**Correspondence email*: *abrarr@ft.untar.ac.id*

Received: 23/05/2026 Revised: 06/06/2026 Accepted: 14/06/2026

Abstract: Manifolds are crucial components in various industries, particularly in oil and gas, agriculture, and energy distribution, where they function to combine fluid flow from multiple pathways into a single header pipe. Achieving uniform flow distribution is essential for maintaining system efficiency and reliability. However, non-uniform flow distribution frequently occurs due to differences in flow resistance, system geometry, and inter-stream interactions at each junction. To address the limitations of simplified analytical approaches such as the Bernoulli equation, which does not simultaneously accommodate viscosity, turbulence, and compressibility effects, a numerical approach based on Computational Fluid Dynamics was employed. This study aims to analyze the flow distribution characteristics, including velocity, pressure, and mass flow rate, in a seven inlet collector manifold, while comparing simulation results with the Bernoulli equation prediction and demonstrating consistency with the governing Navier–Stokes framework. Simulations were conducted in three dimensions using ANSYS Fluent with the SST k-ω turbulence model and the Peng–Robinson real gas model for methane at 136 bar and 70°C. Results revealed progressive flow maldistribution, with velocity increasing from 50 m/s at the inlets to 73.94 m/s at the outlet, accompanied by a total pressure drop of approximately 542 kPa. Density–velocity and density–total pressure correlations exhibited non-linear interdependencies consistent with the Navier–Stokes equations, confirming the significant roles of viscosity, turbulence, and compressibility effects within the system.

Keywords: flow; manifold; SST k-ω; turbulence; CFD

9 INDUSTRY, INNOVATION AND INFRASTRUCTURE

SDGs Problem Solving

This study contributes to SDGs Chapter #9 by using Computational Fluid Dynamics (CFD) to optimize the flow of the gas manifold thus improving the efficiency, reliability and sustainability of industrial pipe systems through advanced engineering analysis of non-uniform flow distribution and pressure loss.

Conflict of Interest Statement: The author(s) declares that the research was conducted in the absence of any commercial or financial relationship that could be construed as a potential conflict of interest.

Jurnal Asiimetrik: Jurnal Ilmiah Rekayasa dan Inovasi - ASIIMETRIK is an open access and peer-reviewed journal published by Faculty of Engineering, Universitas Pancasila, Indonesia.

1. INTRODUCTION

Manifolds are crucial components across various industries, particularly in oil and gas, agriculture, and energy distribution. The primary function of a manifold is to distribute or collect fluid flow from multiple pathways and ensure uniform fluid flow distribution to maintain system efficiency (Sotoodeh, 2020; Yazici *et al.*, 2024; Bridge, 2025). However, achieving uniform flow distribution presents a significant challenge due to the complex interactions between fluid flow and system geometry (Zhang *et al.*, 2023).

In the oil and gas sector, manifolds are employed across multiple stages of production and transportation, including wellhead gathering systems, separation trains, and gas compression networks. The reliability of manifold performance is directly tied to operational safety and production efficiency. In high-pressure gas transmission applications such as the one examined in this study, operating pressures can reach or exceed 100 bar, making accurate flow modeling particularly important. Under such conditions, gas behavior deviates significantly from ideal assumptions, necessitating the use of real gas equations of state to accurately predict thermodynamic properties such as density and viscosity. Failure to account for these deviations can result in significant errors in predicted flow rates, pressure drops, and energy consumption (Garbai, Santa and Bošnjaković, 2025).

Non-uniform flow distribution is a common issue in manifold systems, caused by the accumulation of flow from multiple inlets, which increases flow velocity and induces pressure differentials. This progressive increase in mass flow rate along the manifold results in velocity and pressure variations that contribute to uneven flow distribution across each inlet (Ganguli and Pandit, 2022). This is consistent with the findings by Sparrow *et al.,* who reported that flow accumulation along the manifold causes flow acceleration, which in turn contributes to non-uniform pressure and triggers uneven flow distribution (Sparrow, Tong and Abraham, 2006).

Beyond pressure variation, the balance between momentum and frictional forces plays a critical role in determining flow distribution uniformity. At higher Reynolds numbers, the dominance of inertial forces tends to improve flow uniformity, whereas at lower Reynolds numbers, viscous effects tend to exacerbate distributional non-uniformity. Furthermore, geometric parameters such as the number of inlets, inlet spacing, and inlet positioning have been identified as key factors influencing flow behavior. Increasing the number of inlets generally leads to more complex flow interactions and greater non-uniformity (Li and Park, 2025). In collector type manifold, where multiple lateral pipes discharge into a common header, these geometric and fluid-dynamic interactions become particularly pronounced as flows from adjacent inlets merge and generate competing momentum vectors within the header pipe.

Flow interactions at junctions also contribute significantly to flow complexity. As multiple streams enter the manifold, they interact and generate vortices and recirculation zones. These phenomena not only disrupt velocity distribution but also increase energy losses within the system (Luaibi and Abdulwahid, 2022). In certain cases, the interaction between high-velocity streams can induce jet impingement effects, resulting in localized regions of elevated pressure and turbulence (Rachdi *et al.*, 2025). The jet impingement phenomenon is particularly significant in systems where the inlet pipe diameter is substantially smaller than the header pipe diameter, as the sudden area expansion causes the entering fluid to form a free jet that impinges on the opposing header wall or on the existing flow within the header. This interaction generates strong turbulent mixing and localized pressure fluctuations that propagate along the manifold and affect the behavior of subsequent inlets.

The consequences of non-uniform flow distribution extend beyond fluid behavior alone. Uneven flow distribution can lead to increased pressure drop, reduced system efficiency, and potential structural damage resulting from uneven loading conditions (Singh, Gill and Vasudev, 2023; Li *et al.*, 2024).

Sparrow *et al.,* developed a quasi-analytical method for multi-inlet manifolds based on momentum balance and empirical loss coefficients (Sparrow, Tong and Abraham, 2006). While this approach captures the gross flow accumulation effect, it assumes one-dimensional flow and does not account for turbulence or compressibility, limiting its accuracy at high Reynolds numbers. Yazici *et al.,* applied CFD to examine uniformity in several manifold geometries, demonstrating improved distribution through outlet-side modifications, but their study was conducted at low pressure with incompressible assumptions (Yazici *et al.*, 2024). Ganguli and Pandit, used CFD to optimize a central-inlet–outlet manifold, but their geometry differs substantially from collector-type manifolds used in oil and gas (Ganguli and Pandit, 2022). The Bernoulli equation has been used as a simplified analytical benchmark for pressure-velocity relationships in pipe flow. However, it is restricted to steady, inviscid, incompressible flow along a single streamline and cannot simultaneously account for viscous losses, turbulent mixing, and real-gas compressibility effects that are dominant in the present high-pressure methane system.

To investigate the phenomenon of fluid flow distribution, numerical methods employing CFD represent an effective approach for analyzing such phenomena in detail. CFD enables the simultaneous resolution of the coupled governing equations of mass, momentum, and energy conservation across a three-dimensional computational domain, capturing the full complexity of turbulent flow in complex geometries. Unlike simplified analytical methods, CFD can accommodate viscosity, turbulence, compressibility, and real gas behavior within a unified simulation framework. Through CFD, velocity distribution, pressure fields, and flow patterns can be observed both visually and quantitatively. This study aims to analyze flow distribution in a seven-inlet manifold by examining velocity and pressure contours, mass flow rates, while benchmarking pressure drop predictions with the Bernoulli equation and demonstrating that the observed non-linearities are consistent with the Navier–Stokes governing equations.

The fluid assumptions and boundary conditions adopted in this study involve methane flowing under high-pressure conditions at 136 bar and an operating temperature of 70°C. Although the operating pressure is relatively high, the thermodynamic state of the system is maintained within the gas phase, away from phase-change conditions such as condensation or solidification (ToolBox, 2008; Wang *et al.*, 2026). These boundary conditions were established to ensure that the density variations observed in the simulation are attributable solely to the compressibility effects of the gas, without interference from phase transition phenomena. Consequently, the model remains valid in representing the flow behavior of gas within the manifold system.

2. METHODOLOGY

The present study was conducted with CFD simulation. The variables examined in this study include velocity, static pressure, density, and mass flow rate. The manifold geometry was designed in three dimensions using Autodesk Inventor, while the CFD simulation was performed in three dimensions using ANSYS Student R2 2025. All simulations were executed on a workstation equipped with an AMD Ryzen 9 5900HX processor with Radeon Graphics.

The research procedure is as followed. The process begins with geometry modeling of the seven-inlet collector manifold in Autodesk Inventor, followed by meshing using a polyhedral element scheme in ANSYS Fluent with mesh independence verification. Boundary conditions are then defined according to the operating parameters (methane Real-Gas Peng Robinson, 136 bar, 70°C, 50 m/s inlet velocity), after which the CFD simulation is executed using the SST k-ω turbulence model. Finally, post processing is performed to extract velocity, pressure, density, and mass flow rate data, which are compared against theoretical benchmarks (Bernoulli equation and Navier–Stokes equations) for validation.

2.1. Geometry Model

The manifold employed in this study is a collector type manifold, designed to combine fluid flow from multiple branches into a single main stream (Yazici *et al.*, 2024). In Figure 1 the system consists of seven inlet, each with a Nominal Pipe Size (NPS) of 8 inch, connected horizontally to a header pipe with a NPS 20 inch. All flow from the inlets is collected within the header and directed toward a single outlet of also NPS 20 inch (Figure 2). The collector configuration reflects typical subsea and topside gathering manifold arrangements employed in oil and gas production facilities, where multiple wellstreams are combined prior to processing.

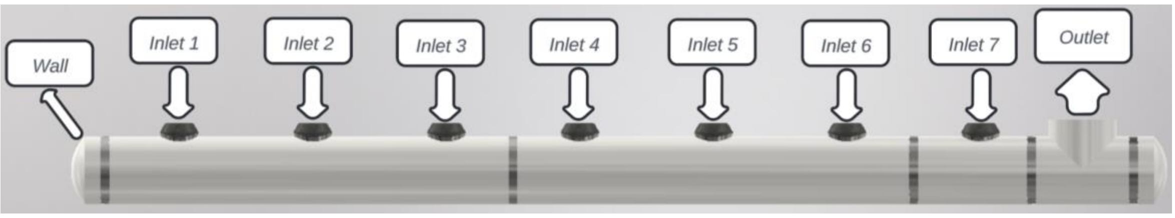

Figure 1. Manifold geometry

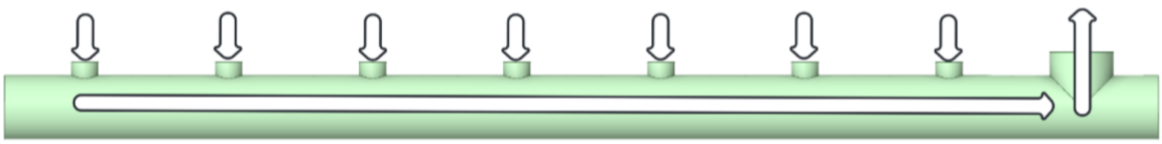

Figure 2. Manifold fluid flow

The inlet pipes are arranged at equal spacing along the header pipe and are oriented perpendicular to the header axis. This orthogonal arrangement, commonly referred to as a T-junction configuration, is representative of industrial practice but introduces a geometric discontinuity that promotes jet impingement, flow separation, and recirculation within the header. The end of the header opposite to the outlet is closed with a wall boundary, creating a dead-end collector geometry in which all flow must exit through the single outlet. This geometry maximizes the accumulation effect and provides a physically meaningful test case for evaluating flow maldistribution phenomena.

2.2. Geometry Model

Meshing is the process of dividing the computational domain into a finite number of discrete elements. In CFD simulations, the choice of mesh type and element size is crucial, as it significantly influences both the accuracy of the solution and the convergence behavior of the numerical computation. The mesh configuration adopted in this study is summarized in Table 1.

Table 1. Mesh configuration

Nodes	Values
Mesh type	Polyhedral
Surface growth rate	Default
Minimum mesh size	0.0002
Maximum mesh size	0.1024
Cells	20,935

A polyhedral mesh type was selected due to its suitability for generating complex mesh models, its efficiency in construction, and its ability to produce fewer mesh cells compared to other mesh types, thereby promoting more stable convergence and improved computational efficiency (Budiarso *et al.*, 2015; Utama *et al.*, 2025).

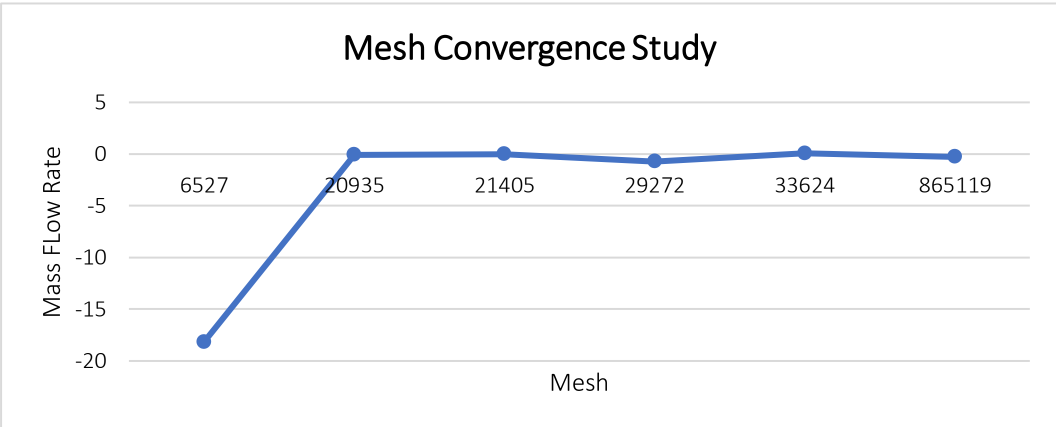

Figure 3. Mesh convergence study

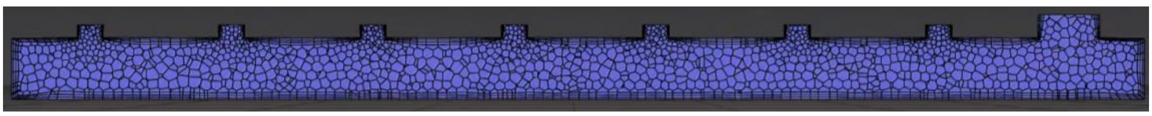

Figure 4. Manifold mesh

To ensure that the simulation result independent, a mesh convergence study was conducted with 6 mesh variation (see Figure 3). The mesh range between 20,935 until 865,199 mesh the flux value of mass flow has the deviation of 0.18%. Considering the computation power efficiency, hence the 20,935 cell is selected and the minimum orthogonal quality obtained from the mesh was 0.395 (see Figure 4).

Boundary conditions were defined to establish the parameters used in the CFD simulation. The fluid domain parameters are presented in Table 2, which contains the variables for the desired model.

Table 2. Boundary conditions

Parameter/Boundary	Values
Inlet (7x)	Velocity Inlet 50 m/s
Outlet	Pressure Outlet Gauge = 0 Pa
Pipe Wall	No Slip
Turbulence model	SST K- ω
Method	Hybrid
Fluid	Methane 70˚C at inlet
Density	Real gas peng-Robinson
Operating Pressure	136 bars
Inlet velocity	50 m/s
Outlet	Pressure outlet

The SST k-ω model was selected as the turbulence computation model, given that the fluid flow within the manifold system is turbulent in nature due to high velocities, changes in flow direction, and inter-stream interactions at each junction. The Reynolds number at the manifold, estimated based on the parameters is 107, confirming fully turbulent flow conditions. The SST k-ω model provides more accurate predictions in both near wall regions and throughout the overall flow field by blending the k-ω formulation in the viscous sublayer with the k-ε model in the free stream, making it particularly suitable for flows with adverse pressure gradients and flow separation (Budiarso *et al.*, 2015; Utama *et al.*, 2025).

$$\frac{\partial}{\partial t}(\rho k) + \frac{\partial}{\partial x_i}(\rho k u_i) = \frac{\partial}{\partial x_j}\left[\boldsymbol{\Gamma}_k \frac{\partial k}{\partial x_j}\right] + G_k - Y_k \tag{1}$$

$$\frac{\partial}{\partial t}(\rho \omega) + \frac{\partial}{\partial x_i}(\rho \omega u_i) = \frac{\partial}{\partial x_j}\left[\boldsymbol{\Gamma}_\omega \frac{\partial \omega}{\partial x_j}\right] + G_\omega - Y_\omega + D_\omega \tag{2}$$

where G_k represents the generation of k due to mean velocity gradients, G_ω represents the generation of ω, Γ_k and Γ_ω represent the effective diffusivity of k and ω, respectively. Y_k and Y_ω represent the dissipation of k and ω in the turbulence (Adanta, Fattah and Muhammad, 2020).

Under high-pressure conditions, the ideal gas assumption becomes inaccurate due to intermolecular interactions within the fluid. Therefore, a real gas model based on the Peng–Robinson Equation of State was employed to more realistically represent the relationship between pressure, temperature, and density. This model can capture non-ideal fluid behavior, including density variations induced by pressure changes, making it well-suited for compressible flow analysis in manifold systems. The working fluid used in this simulation is methane in the gas phase at an operating temperature of 70°C.

$$P = \frac{RT}{\tilde{v}-b} - \frac{\alpha a}{\tilde{v}^2+2b\tilde{v}-b^2} \tag{3}$$

where P is the pressure (Pa), R is the universal gas constant (J/mol.K), T is the temperature (K), $\tilde{v}$ is the molar volume (m^3/mol), b is the co-volume constant representing the excluded volume due to finite molecular size (m^3/mol), α is the dimensionless temperature dependent correction factor that accounts for the attractive forces between molecules, and a is the attraction parameter representing the magnitude of intermolecular attractive forces (Pa.m^6/mol^2) (Adewumi, 2026).

3. RESULTS AND DISCUSSION

Table 3 summarizes the manifold simulation results obtained from CFD analysis using ANSYS Fluent with the SST k-ω turbulence model and the Peng–Robinson real gas density approach for methane at an operating temperature of 70°C and operating pressure at 136 bars. The simulation results are presented in terms of velocity, static pressure, density, and mass flow rate, as detailed in Table 3.

Table 3. Simulation result

Parameter	Inlet Values	Outlet Values	Average
Velocity (m/s)	50	73.940814	60.506385
Static Pressure (Pa)	540,115.79	-2,697.3111	301,903.19
Density (kg/m^3)	89.42383	86.626701	88.196315
Mass Flow Rate (kg/s)	841.15654	-841.21677	-0.06022847
Velocity (m/s)	50	73.940814	60.506385

3.1. Velocity Distribution

The fluid velocity distribution within the manifold exhibits non-uniform characteristics, as illustrated in Figure 5. This phenomenon is consistent with the findings of Yazici *et al.*, who reported that in straight manifold configurations, flow tends to concentrate in regions near the outlet, while other areas experience lower velocities due to flow separation (Yazici *et al.*, 2024).

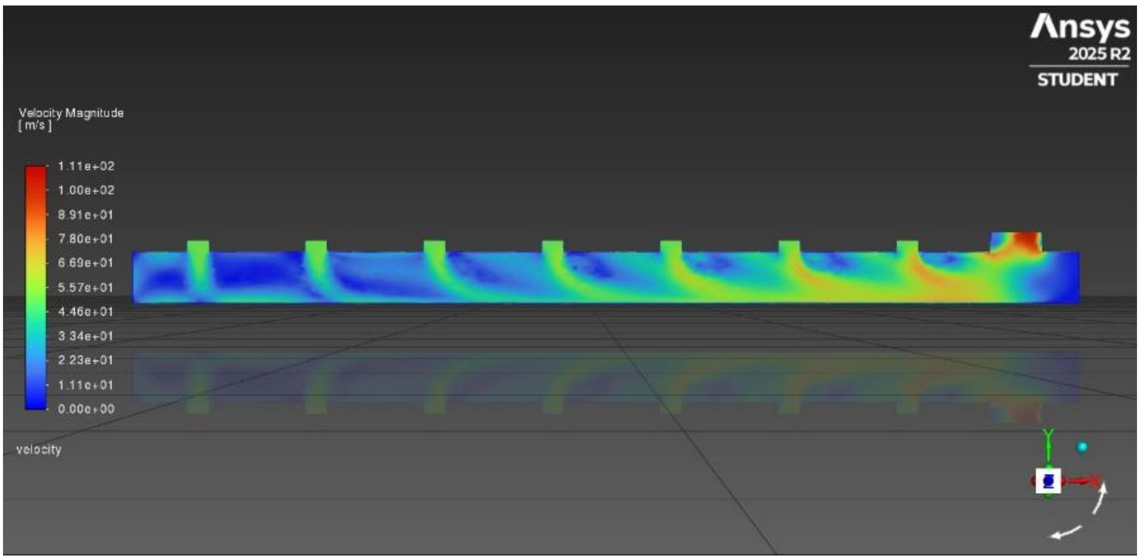

Figure 5. Velocity contour

At each junction between the NPS 8 inlet pipes and the NPS 20 header, jet impingement phenomena were observed as shown in Figure 6. Fluid enters the header at high velocity through the smaller cross-sectional area, generating localized high-velocity zones, as evidenced by the green-to-orange regions in the velocity contour. The cross-sectional area ratio difference causes the fluid to jet into the header, inducing sharp velocity gradients.

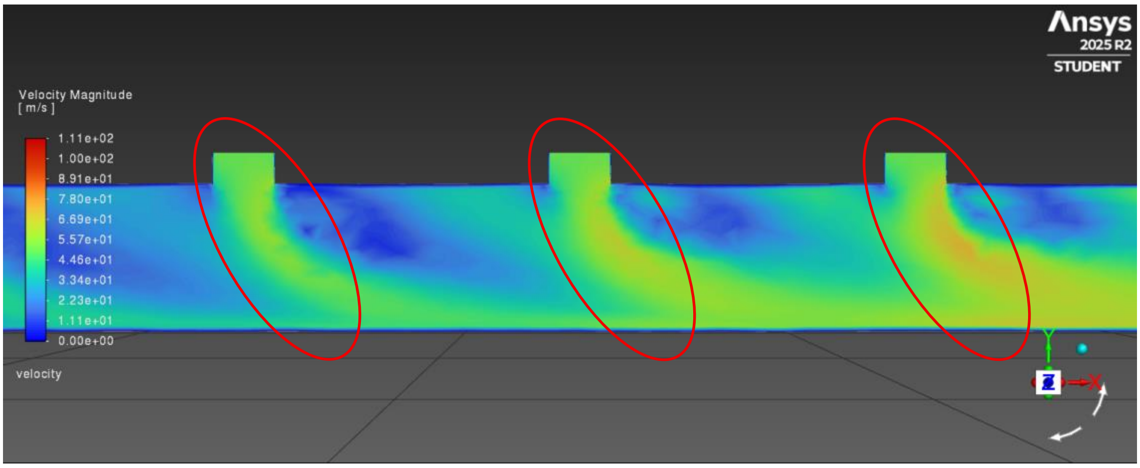

Figure 6. Jet impingement

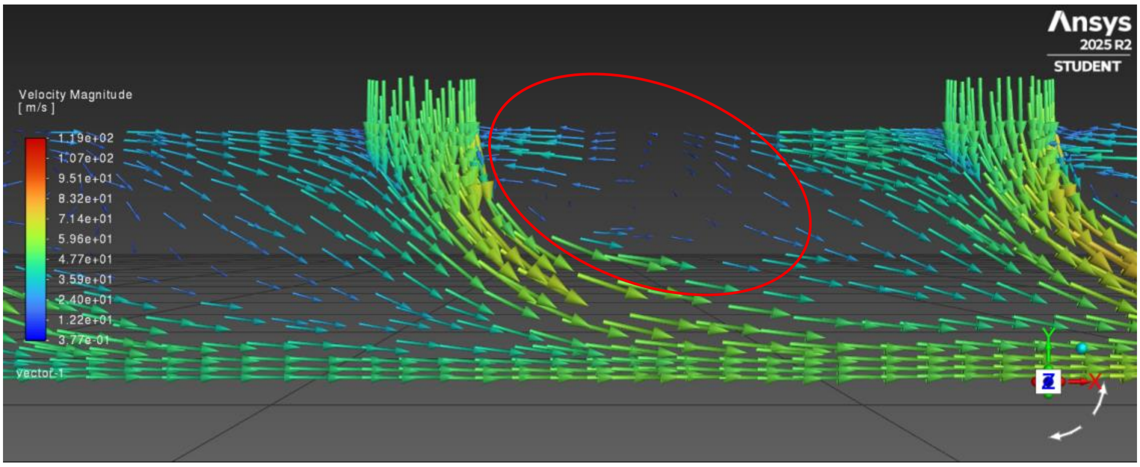

Figure 7. Recirculation zone

In addition, recirculation zones were formed between each inlet as shown in Figure 7, indicated by the dark blue regions in the contour. These zones result from flow separation and sudden expansion as fluid from the inlets enters the larger header. Flow that is unable to follow the wall contour generates wake regions occupied by vortices. Zhou *et al.* noted that vortices at T-junctions exert a significant influence on flow and pressure distribution (Zhou *et al.*, 2017). These vortices are responsible for the non-uniform flow distribution observed along the manifold.

The progressive increase in velocity from the inlets toward the outlet is a direct consequence of the principle of mass conservation. As the cumulative mass flow rate from each inlet increases within a header of constant cross-sectional area, the mean fluid velocity rises accordingly, consistent with the continuity equation (Munson, Rothmayer and Okiishi, 2012):

$$\dot{m} = \rho Q = \rho A V \tag{4}$$

The simulation results presented in Table 3 indicate that velocity increases from 50 m/s at the inlets to 73.94 m/s at the outlet, with an average velocity of 60.51 m/s. More detailed examination of the velocity at each individual inlet reveals a non-uniform distribution pattern. Inlets 1 through 5, located farther from the outlet, exhibit relatively comparable velocities ranging from 49.86 m/s to 51.87 m/s, indicating a stable flow regime in the upstream region of the header. In contrast, a pronounced velocity increase is observed at Inlet 6 and Inlet 7, recording velocities of 58.59 m/s and 63.78 m/s (Figure 8), respectively. This progressive acceleration toward the outlet is attributable to cumulative flow accumulation along the header, wherein the momentum carried by upstream flows compounds at downstream junctions. The larger pressure differential between the inlet pipe and the lower-pressure region near the outlet further drives fluid entry at higher velocities at downstream positions. This behaviour is consistent with the findings of Sparrow *et al.* who reported that flow accumulation along the manifold induces progressive velocity increases at junctions positioned closest to the outlet, thereby contributing to flow maldistribution within the system (Sparrow, Tong and Abraham, 2006).

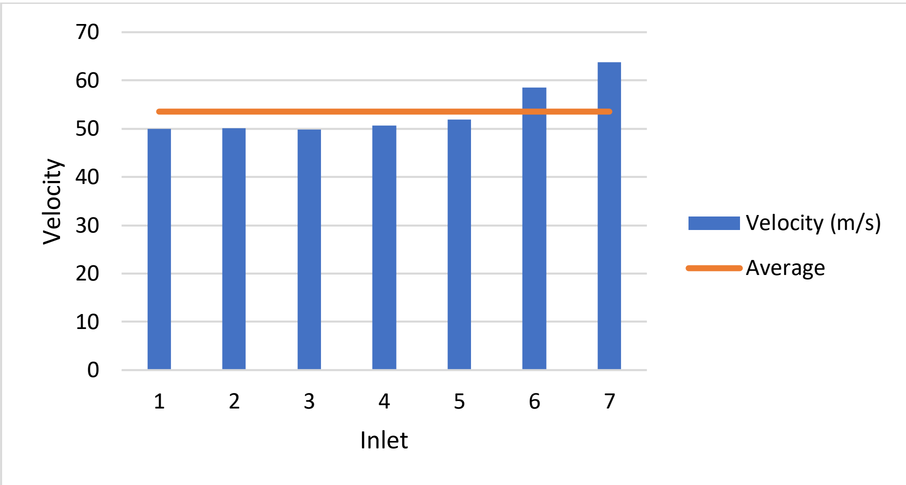

Figure 8. Graph of velocity on each inlet and the velocity average value

3.2. Velocity and Pressure Correlation

The static pressure distribution within the manifold exhibits a strong correlation with the velocity distribution. In regions of high velocity, static pressure tends to decrease, whereas in low-velocity regions such as recirculation zones, static pressure is relatively higher locally. This phenomenon is consistent with the fundamental principles of fluid mechanics, wherein an increase in kinetic energy is accompanied by a reduction in static pressure (Munson, Rothmayer and Okiishi, 2012).

As shown in Figure 7, in the jet regions surrounding the inlets, the increase in velocity leads to a reduction in static pressure, reflected in the pressure contour as lower pressure gradients Figure 9. Conversely, in recirculation zones characterized by low velocity, static pressure tends to remain more stable or increase slightly due to local flow deceleration effects.

Luaibi and Abdulwahidchas studied highlighted that flow interactions at branching junctions, such as T-junctions, can lead to the formation of vortices and recirculation regions (Luaibi and Abdulwahid, 2022). This condition becomes more pronounced in non-uniform flow distribution, where differences in flow rates cause the fluid to deviate from the primary flow path. The resulting vortices and recirculation zones affect the main flow and contribute to pressure drop across the system (Nuryoto *et al.*, 2024; Abuyousseff *et al.*, 2026).

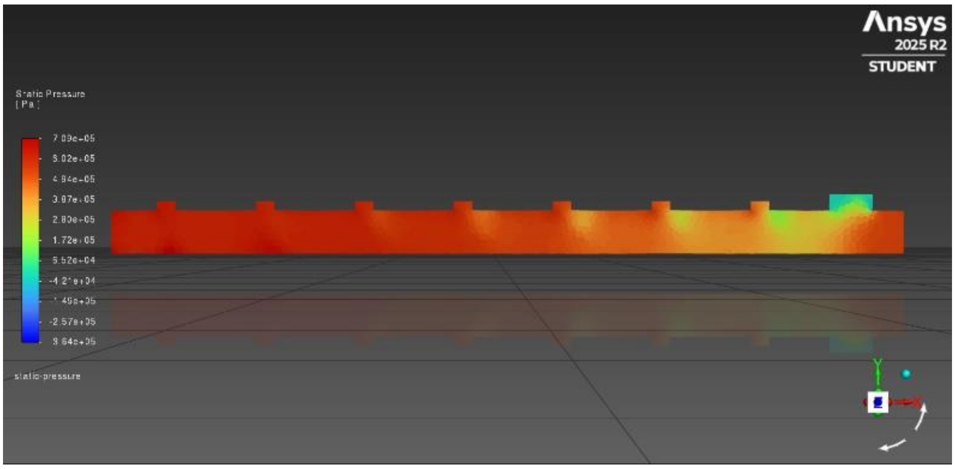

Figure 9. Static pressure contour

3.3. Density

As presented in Table 3, the fluid density decreases from 89.42383 kg/m³ at the inlet to 86.626701 kg/m³ at the outlet, indicating the presence of compressibility effects within the system. This variation is attributed to changes in flow pressure and velocity, whereby the increase in velocity is accompanied by a reduction in static pressure, leading to fluid expansion as the flow transitions from the NPS 8 inlets to the NPS 20 outlet, and a consequent decrease in density (see Figure 10). Fluid density within pipe flow is strongly governed by pressure and velocity variations, a phenomenon discussed by Garbai and Santa in the context of polytropic gas flow analysis in pipelines (Garbai, Santa and Bošnjaković, 2025).

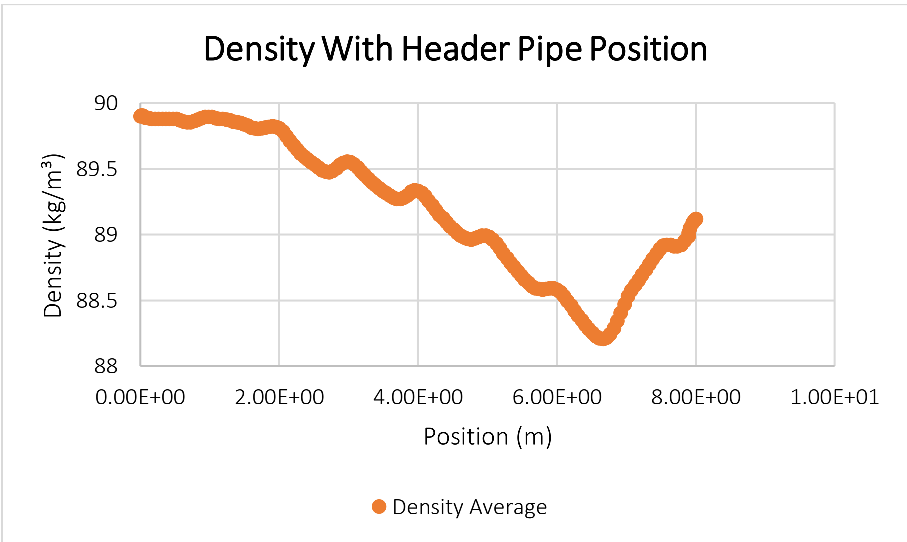

Figure 10. Graph of change in density respect to position of the header pipe

3.4. The Effect of Temperature Variant to Viscosity

The relationship between temperature and molecular viscosity of the fluid is presented in Table 4. Inlet temperature variations were applied over a range of 50°C, 60°C, 70°C, and 80°C to examine the corresponding changes in fluid viscosity. The simulation results indicate that viscosity increases progressively with rising temperature. At 50°C, the viscosity was recorded at 1.12966×10^{-5} Pa·s, increasing to 1.1601×10^{-5} Pa·s at 60°C, 1.19015×10^{-5} Pa·s at 70°C, and reaching 1.2198×10^{-5} Pa·s at 80°C. This trend reflects a linear relationship between temperature and viscosity within the examined range.

Table 4. Temperature variations effect toward molecular viscosity

Temperature (°C)	Molecular Viscosity (Pa.s)
50	1.12966×10^{-5}
60	1.1601×10^{-5}
70	1.19015×10^{-5}
80	1.2198×10^{-5}

This phenomenon is consistent with the behavior of gaseous fluids, in which rising temperature increases the kinetic energy of molecules, thereby intensifying intermolecular collisions and momentum transfer. This results in greater resistance to flow deformation, which is defined as viscosity (Munson, Rothmayer and Okiishi, 2012). Furthermore, the results demonstrate a relatively linear change in viscosity across the temperature range examined, suggesting that within the 50°C to 80°C range, the influence of temperature on viscosity has not yet exhibited significant non-linearity (see Figure 11).

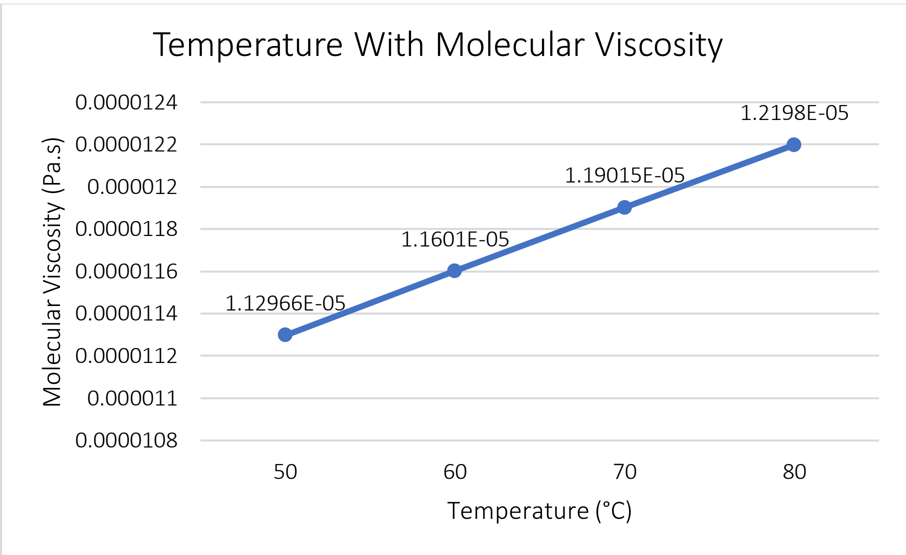

Figure 11. Graph of change in viscosity to temperature difference

3.5. Velocity Distribution

To validate that the simulation results accurately represent real flow behavior, a correlation analysis was conducted among the density, velocity, and total pressure values obtained from the simulation data.

$$\rho\left(\frac{\partial v}{\partial t} + v\ .\ \nabla v\right) = -\nabla P + \mu \nabla^2 v + \rho g \tag{5}$$

Where ρ is the fluid density (kg/m^3), $\vec{v}$ is the velocity vector (m/s), t represents time (s). The pressure is denoted by P (Pa), μ is dynamic viscosity (Pa.s), and g is gravitational acceleration (m/s^2). The term

∇P represents the pressure gradient (Pa/m), while $\nabla^2 v$ represents the viscous diffusion of momentum.

3.5.1. Density-Velocity Correlation

The relationship between density and velocity exhibits an inverse trend, wherein an increase in velocity is accompanied by a decrease in fluid density. This phenomenon indicates the presence of fluid compressibility effects, consistent with the real gas model employed in this study, namely the Peng–Robinson Equation of State. Physically, as the fluid accelerates, the local pressure tends to decrease, which in turn causes a corresponding reduction in fluid density (see Figure 12).

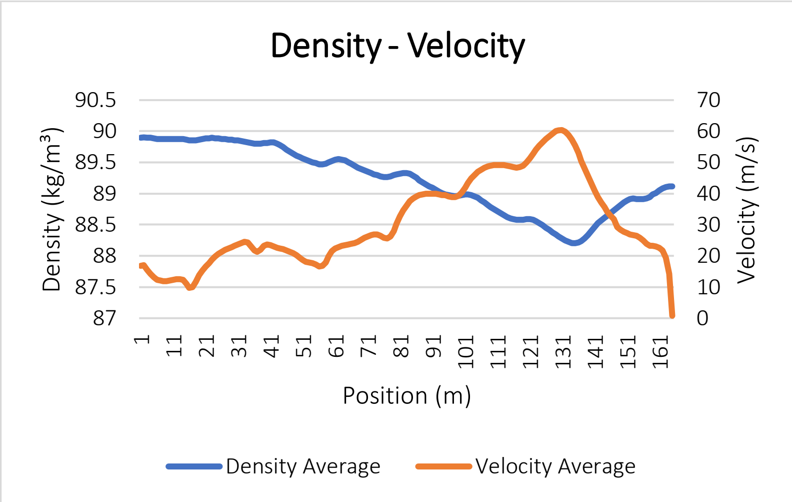

Figure 12. Graph of Density – Velocity Correlation

3.5.2. Density-Total Pressure Correlation

The relationship between density and total pressure demonstrates a direct proportional trend, wherein an increase in total pressure is accompanied by an increase in fluid density. This indicates that total pressure serves as an indicator of the total energy within the system and directly influences the thermodynamic state of the fluid. In the context of a real gas, an increase in pressure results in a corresponding increase in fluid density (see Figure 13).

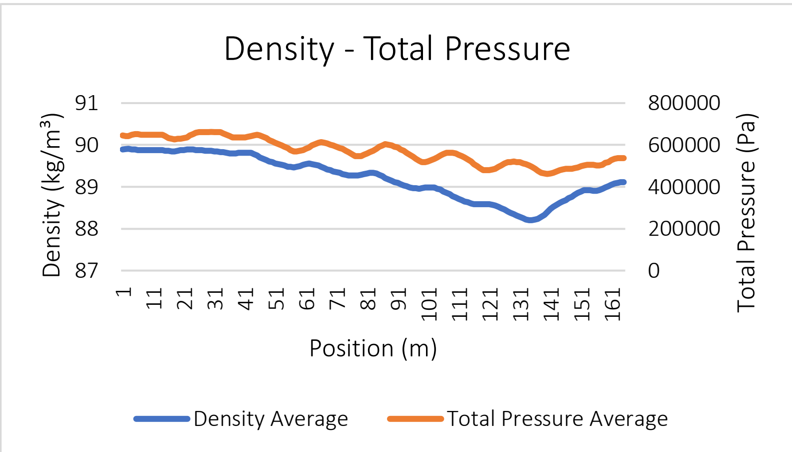

Figure 13. Graph of Density – Total Pressure Correlation

3.5.3. Interpretation With Respect to Navier-Stokes Equation

The correlations observed among density, velocity, and total pressure suggest that the flow in this experiment does not conform to the ideal assumptions underlying the Bernoulli equation. Instead, the results exhibit non-linear interdependencies characteristic of viscous, turbulent flow, as described by the Navier–Stokes equations (Buya, 2025).

3.6. Pressure Drop Analysis

The simulation results indicate that static pressure decreases from 540,115.79 Pa (gauge) at the inlet to −2,697.31 Pa at the outlet. Considering the operating pressure of 13.6 MPa, the total pressure drops across the system is calculated approximately 542 kPa. When compared to the system operating pressure, this pressure drop corresponds to approximately 4% of the total pressure. The observed pressure drop represents the cumulative contribution of several energy loss mechanisms, namely:

- Major losses, arising from frictional resistance along the pipe walls.
- Minor losses, resulting from flow direction changes at the junctions.
- Turbulent losses, caused by inter-stream interactions.

3.7. Comparison With Theoretical Approaches

When analyzed using an idealized approach, the relationship between velocity and pressure can be described by the Bernoulli equation. However, this approach assumes inviscid flow with no energy losses.

$$P_{inlet} + \frac{1}{2}\rho_{inlet} v_{inlet}^2 = P_{outlet} + \frac{1}{2}\rho_{outlet} v_{outlet}^2 \tag{5}$$

where P is pressure (Pa), ρ is the fluid density (kg/m^3), v is the velocity (m/s).

In the present case, the velocity increase from 50 m/s to 73.94 m/s would, under ideal conditions, produce a predicted pressure drop of 417.8 kPa. Nevertheless, the simulation results reveal a substantially greater pressure drop of 542 kPa, indicating the presence of significant energy losses within the system. The difference between the Bernoulli predicted pressure drop and CFD obtained pressure drop yields an excess pressure drop of approximately 23 %. This excess loss is attributed to viscous dissipation, flow mixing, and flow separation at the T-junctions, effects that are inherently absent from the Bernoulli equation.

3.8. Non-Linear Interdependency Analysis of Flow Parameters Based on Navier–Stokes Equations

The relationships among density, velocity, and total pressure obtained from the simulation results do not exhibit a simple linear pattern; rather, they demonstrate complex and mutually dependent interactions (Herrero *et al.*, 2012). The simulation results reveal significant deviations, as evidenced by density variations (Figure 13) attributable to pressure changes and inter-stream interactions within the manifold.

Within the framework of the Navier–Stokes equations, this phenomenon can be explained through the presence of the non-linear convective momentum term $\left(\frac{\partial v}{\partial t} + v \, . \, \nabla v\right)$, which represents the interaction among velocity components within the flow field (Herrero *et al.*, 2012). This term causes the velocity change at any given point to depend not only on local conditions, but also on the surrounding velocity distribution. This is consistent with the simulation results, which demonstrate the occurrence of jet impingement (Figure 6), vortex formation, and recirculation zones (Figure 7) arising from the interaction of flows from multiple inlets.

Furthermore, the contribution of viscosity represented by the momentum diffusion term $(\mu\nabla^2 v)$, along with turbulent effects modeled using the SST k–ω turbulence model, further reinforces the non-linear nature of the relationships among flow parameters. Turbulence induces velocity fluctuations and increases energy dissipation, which affects the overall pressure and density distribution. Additionally, the application of the Peng–Robinson real gas model demonstrates that density is not constant, but rather dependent on pressure and temperature, further adding to the complexity of the inter-variable relationship (Sirignano, 2018).

Accordingly, the interdependencies among density, velocity, and pressure within this manifold system cannot be adequately described using a simple linear approach but must instead be understood as the result of non-linear interactions characteristic of real fluid flow.

3.9. Non-Uniform Flow Distribution

The uneven velocity distribution within the manifold indicates the presence of a non-uniform flow distribution phenomenon. Inlets located closer to the outlet tend to exhibit higher velocities compared to those situated farther upstream (see Table 5).

Table 5. Point in each area near the inlet

Inlet	Velocity (m/s)	Average
1	49.935787	
2	50.128699	
3	49.864572	
4	50.685941	53.55398
5	51.87776	
6	58.59893	
7	63.786136	

The ratio between highest velocity value on inlet 7, 63.78 m/s and lowest on inlet 3, 49.86 m/s is 1.28. This shows that inlet closer to the outlet carry 28% more methane than the other inlet. This phenomenon is attributed to pressure distribution differences along the header, where the lower pressure near the outlet draws flow more strongly than the upstream region (Sparrow, Tong and Abraham, 2006). As a result, an imbalance in flow distribution occurs, which can adversely affect the overall system performance. This condition may lead to:

- A reduction in system efficiency.
- An increase in energy losses.
- A potential imbalance in fluid distribution.

4. CONCLUSION

The CFD simulation of a seven-inlet collector manifold for methane gas at 136 bar and 70°C successfully demonstrated the presence of uneven flow distribution, where inlets closer to the outlet exhibited significantly higher velocities up to 63.78 m/s compared to upstream inlets 49.93 m/s. The total pressure drop of 542 kPa exceeded the Bernoulli-predicted value by approximately 77%, confirming the dominant role of viscous dissipation, jet impingement, and recirculation losses. Fluid density decreased from 89.42 kg/m³ to 86.62 kg/m³, validating the compressibility effects captured by the Peng–Robinson real gas model.

REFERENCES

Abuyousseff, A.S. *et al.* (2026) 'Investigation of Leaking Compressed Hydrogen in Piping Lines Using Peng-Robinson EOS.: Case Study', *Journal of Engineering Research*, 9(4), pp. 1–10. Available at: https://doi.org/10.21608/jer.2026.458858.1027.

Adanta, D., Fattah, I.M.R. and Muhammad, N.M. (2020) 'Comparison of Standard k-epsilon and SST k-omega Turbulence Model for Breastshot Waterwheel Simulation', *Journal of Mechanical Science and Engineering*, 7(2), pp. 039–044. Available at: https://doi.org/10.36706/jmse.v7i2.44.

Adewumi, M. (2026) 'Peng-Robinson EOS'. Pennsylvania, USA: The Pennsylvania State University. Available at: https://courses.ems.psu.edu/png520/m11_p2.html (Accessed: 15 May 2026).

Bridge, C. (2025) 'Overview of Oil and Gas Production'. ResearchGate. Available at: https://doi.org/DOI:10.13140/RG.2.2.29285.31204.

Budiarso, B. *et al.* (2015) 'Inverse-Turbulent Prandtl Number Effects on Reynolds Numbers of RNG k-ε Turbulence Model on Cylindrical-Curved Pipe', *Applied Mechanics and Materials*, 758, pp. 35–44. Available at: https://doi.org/10.4028/www.scientific.net/AMM.758.35.

Buya, S.B. (2025) 'Bridging the Bernoulli Equation and the Navier-Stokes Equation'. ResearchGate. Available at: https://doi.org/10.13140/RG.2.2.32966.59204.

Ganguli, A.A. and Pandit, A.B. (2022) 'Computational Fluid Dynamics Simulations to Improve Performance Characteristics of a Manifold Having a Central Inlet and Outlet', *Frontiers in Energy Research*, 10, pp. 1–20. Available at: https://doi.org/10.3389/fenrg.2022.1013540.

Garbai, L., Santa, R. and Bošnjaković, M. (2025) 'Advanced Analytical Modeling of Polytropic Gas Flow in Pipelines: Unifying Flow Regimes for Efficient Energy Transport', *Technologies*, 13(11), pp. 1–26. Available at: https://doi.org/10.3390/technologies13110482.

Herrero, R. *et al.* (2012) 'About the Oscillatory Possibilities of the Dynamical Systems', *Physica D: Nonlinear Phenomena*, 241(16), pp. 1358–1391. Available at: https://doi.org/10.1016/j.physd.2012.05.001.

Li, B. and Park, T.S. (2025) 'Effects of Inlet and Outlet Layout on the Outflow Uniformity of Dividing Manifolds', *Journal of Propulsion and Energy*, 5(1), pp. 33–47. Available at: https://doi.org/10.6108/JPNE.2025.5.1.033.

Li, H. *et al.* (2024) 'A Coupled Modeling Framework for Investigating Flow Maldistribution in Cross-Flow-Corrugated Plate Heat Exchangers', *International Journal of Fluid Engineering*, 1(3), p. 034301. Available at: https://doi.org/10.1063/5.0204274.

Luaibi, M. and Abdulwahid, M. (2022) 'Numerical Analysis by Computational Fluid Dynamic Simulation of Fluid Flow in A T- Junction', *Proceedings of 2nd International Multi-Disciplinary Conference Theme: Integrated Sciences and Technologies. 2nd International Multi-Disciplinary Conference Theme: Integrated Sciences and Technologies (IMDC-IST 2021)*, Sakarya, Turkey: EAI. Available at: https://doi.org/http://dx.doi.org/10.4108/eai.7-9-2021.2314888.

Munson, B.R., Rothmayer, A.P. and Okiishi, T.H. (2012) *Fundamentals of Fluid Mechanics*. 7th edn. Wiley. [Print].

Nuryoto, N. *et al.* (2024) 'Observasi Penurunan Tekanan (Pressure Drop) Pada Sistem Perpipaan: Pengaruh Panjang Dan Diameter Pipa, Elbow, Dan Tee', *Jurnal Rekayasa Mesin*, 15(2), pp. 1023–1039. Available at: https://doi.org/10.21776/jrm.v15i2.1666.

Rachdi, Z. *et al.* (2025) 'CFD Analysis of Heat Transfer Enhancement in Impinging Jet Array by Varying Number of Jets and Spacing', *Scientific Reports*, 15(1), pp. 1–17. Available at: https://doi.org/10.1038/s41598-025-86360-w.

Singh, J., Gill, H.S. and Vasudev, H. (2023) 'Computational Fluid Dynamics Analysis on Role of Particulate Shape and Size in Erosion of Pipe Bends', *International Journal on Interactive Design and Manufacturing (IJIDeM)*, 17(5), pp. 2631–2646. Available at: https://doi.org/10.1007/s12008-022-01094-7.

Sirignano, W.A. (2018) 'Compressible Flow at High Pressure with Linear Equation of State', *Journal of Fluid Mechanics*, 843, pp. 244–292. Available at: https://doi.org/10.1017/jfm.2018.166.

Sotoodeh, K. (2020) 'Manifold Technology in the Offshore Industry', *American Journal of Marine Science*, 8(1), pp. 14–19. Available at: https://doi.org/10.12691/marine-8-1-3.

Sparrow, E.M., Tong, J.C.K. and Abraham, J.P. (2006) 'A Quasi-Analytical Method for Fluid Flow in a Multi-Inlet Collection Manifold', *Journal of Fluids Engineering*, 129(5), pp. 579–586. Available at: https://doi.org/10.1115/1.2717620.

ToolBox, T.E. (2008) *Methane (CH_4): Thermophysical Properties and Phase Diagram*. Engineering ToolBox. Available at: https://www.engineeringtoolbox.com/methane-d_1420.html (Accessed: 14 May 2026).

Utama, D.W. *et al.* (2025) 'A CFD Investigation of Piping System Design for a Tank Cleaning Machine', *Engineering, Technology & Applied Science Research*, 15(6), pp. 29418–29427. Available at: https://doi.org/10.48084/etasr.13595.

Wang, M. *et al.* (2026) 'Revisiting the Phase Diagram of Methane', *Physical Review Letters*, 136(4), p. 046101. Available at: https://doi.org/10.1103/7hxd-hhjf.

Yazici, F. *et al.* (2024) 'Examining the Uniformity of Flow Distribution in Manifolds', *Journal of Applied Fluid Mechanics*, 17(5), pp. 989–1001. Available at: https://doi.org/10.47176/jafm.17.05.2302.

Zhang, M. *et al.* (2023) 'Reducing the Flow Maldistribution in Heat Exchangers through a Novel Polymer Manifold: Numerical Evaluation', *Energies*, 16(20), p. 7120. Available at: https://doi.org/10.3390/en16207120.

Zhou, J. *et al.* (2017) 'CFD Simulation for Flow Distribution in Manifolds of Central-Type Compact Parallel Flow Heat Exchangers', *Applied Thermal Engineering*, 126, pp. 670–677. Available at: https://doi.org/10.1016/j.applthermaleng.2017.07.194.